

Particle Physics Research Centre  
School of Physics and Astronomy  
Queen Mary University of London

## **Measurements of $H \rightarrow b\bar{b}$ decays and $VH$ production**

Thomas Charman

Supervisor: Dr. Jonathan Hays

Submitted in partial fulfillment of the requirements of the Degree of Doctor of  
Philosophy May 22, 2020.

I, Thomas Paul Charman, confirm that the research included within this thesis is my own work or that where it has been carried out in collaboration with, or supported by others, that this is duly acknowledged below and my contribution indicated. Previously published material is also acknowledged below.

I attest that I have exercised reasonable care to ensure that the work is original, and does not to the best of my knowledge break any UK law, infringe any third party's copyright or other Intellectual Property Right, or contain any confidential material.

I accept that the College has the right to use plagiarism detection software to check the electronic version of the thesis. I confirm that this thesis has not been previously submitted for the award of a degree by this or any other university.

The copyright of this thesis rests with the author and no quotation from it or information derived from it may be published without the prior written consent of the author.

Signature:

Date:

Details of collaboration and publications:

# Contents

<b>List of Figures</b>	<b>4</b>
<b>List of Tables</b>	<b>5</b>
<b>1 The ATLAS Detector at the Large Hadron Collider</b>	<b>6</b>
1.1 The Large Hadron Collider . . . . .	6
1.2 The ATLAS Detector . . . . .	11
Tracking: The Inner Detector . . . . .	13
Pixel Detectors . . . . .	16
Semiconductor Tracker . . . . .	16
Transition Radiation Tracker . . . . .	18
Calorimeters . . . . .	18
Electromagnetic Calorimeter . . . . .	20
Hadronic Calorimeter . . . . .	20
Muon Spectrometers . . . . .	21
Trigger Systems . . . . .	22

# List of Figures

1.1	The CERN accelerator complex . . . . .	7
1.2	A representation of a pair of idealised cylindrical magnets in a dipole configuration. Two positively charged particles are shown as circles, the red particle is traveling out of the page, the green particle is traveling into the page. The forces experienced by each particle due to the magnetic field are shown as blue arrows. . . . .	8
1.3	A representation of a radio-frequency cavity where the electric field lines are shown in black. . . . .	9
1.4	Representation of an idealised set of coil magnets in a quadrupole configuration with a proton beamspot shown as a red ellipse. The proton beam is drawn coming out of the page ( <i>watch out!</i> ), magnetic field lines are drawn in black and the forces acting on each bunch of protons are drawn as blue arrows. . . . .	10
1.5	The ATLAS Detector . . . . .	11
1.6	ATLAS magnetic field . . . . .	13
1.7	A diagram showing the geometric construction of the sagitta ( $S$ ) of a track. The track is comprised of a sequence of hits marked by crosses and the “lever-arm” distance between the first and last hit in the track is marked $L$ . Charged tracks in a magnetic field pointing into the page, as shown, form arcs of circles. The two lines marked as normal to the track are radii of the circle to which this track’s arc belongs. . . . .	14
1.8	A diagram showing the geometric construction of the impact parameters $d_0$ and $z_0$ . . . . .	15

1.9	ATLAS inner detector	15
1.10	ATLAS long strip module	17
1.11	ATLAS strip close-up	17
1.12	ATLAS Calorimeter	19
1.13	ATLAS muon subsystem	22

## List of Tables

# Chapter 1

## The ATLAS Detector at the Large Hadron Collider

### 1.1 The Large Hadron Collider

The Large Hadron Collider (LHC) [1] is a large circular machine located 100 m underground straddling the Swiss-French border at the European Organisation for Nuclear Research (CERN). The LHC accelerates and collides protons and other charged particles. It has a diameter of 27 km and resides in a tunnel which was originally excavated for the Large Electron-Positron Collider [2] experiment. During its construction the tunnel was the largest civil engineering project in Europe to date. Today there are many physics experiments that take place at CERN, some of which are marked in figure. 1.1. There are currently seven experiments that record data from the collisions at the LHC: ATLAS [3], CMS [4], LHCb [5], ALICE [6], MoEDAL [7], TOTEM [8] and LHCf [9].

The Lorentz force is fundamental to the LHC's accelerator technologies and detectors. Expressed as

$$\vec{F} = q(\vec{E} + \vec{v} \times \vec{B}), \quad (1.1)$$

it is clear that the force due to an electric field  $\vec{E}$  on a particle with charge  $q$  acts in the direction of the velocity of the field whereas the force due to a magnetic field  $\vec{B}$

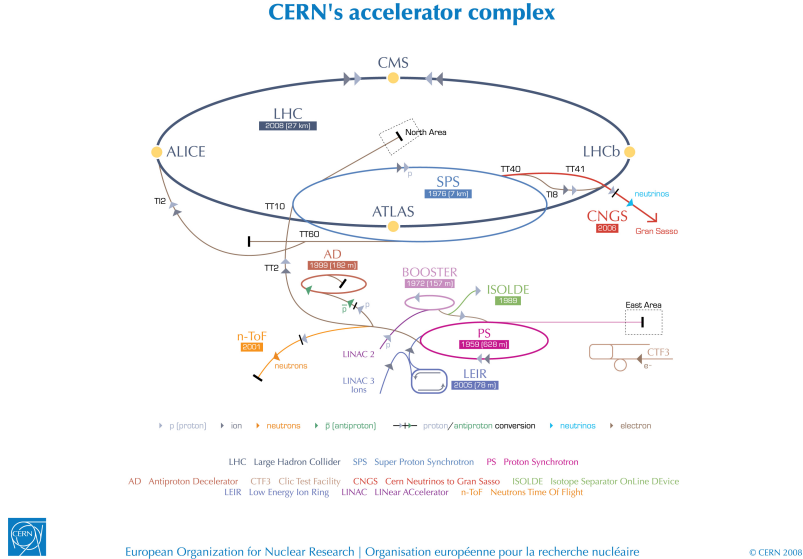


Figure 1.1: The CERN accelerator complex [10].

acts perpendicular to both the field and the velocity of the particle  $\vec{v}$ . It is therefore clear that an electric field may be used to accelerate and give energy to a charged particle whereas a magnetic field will alter the trajectory of a particle whilst keeping its energy constant.

The LHC is a synchrotron, an accelerator that uses magnets in a dipole configuration, such as in figure 1.2, to bend the path of charged particles into conformity with its circular shape. It is apparent from studying the figure that counter-rotating beams of same sign charged particles will require two sets of dipole magnets in order to rotate in opposite directions around the same ring. This is one disadvantage of a proton-proton collider with respect to a proton-anti-proton collider such as the Tevatron [11] which can use the same magnets for both beams. On the other hand, the proton-proton collider is able to separate the beams after they have been brought together to collide with a single dipole. The bending magnets of a synchrotron are designed to ramp up their magnetic field in synchronisation with the kinetic energy of the accelerated particles, allowing higher energies to be achieved before the beam is lost. The LHC can accelerate each beam to an energy of 6.5 TeV leading to collisions with a centre of mass energy of  $\sqrt{s} = 13$  TeV, although the design energy of the LHC is  $\sqrt{s} = 14$  TeV. The Tevatron held the previous record for centre of mass energy of collisions of  $\sqrt{s} = 2$  TeV. The LHC has 1232 dipole magnets [1] which

are made of copper-clad niobium-titanium cables, a superconducting material whose electrical resistance falls to zero below 10 K. In order to maintain super-conductivity a cryogenic system using liquid helium is employed to cool the magnets. The higher the velocity of a charged particle, and the tighter the desired bending radius, the larger the magnetic field required to perform the bending. The large size of the LHC and the choice of superconducting magnet technologies are both informed by the aim to accelerate protons to the highest energy, and therefore velocity, possible.

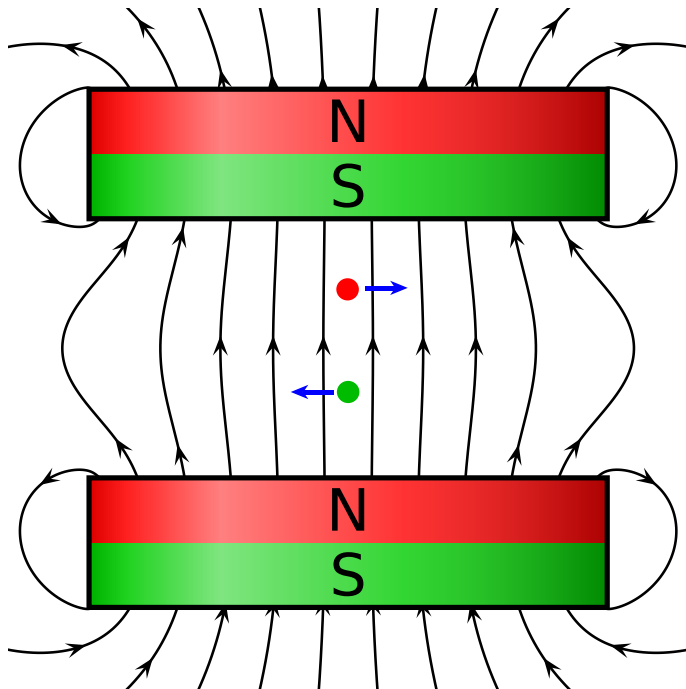


Figure 1.2: A representation of a pair of idealised cylindrical magnets in a dipole configuration. Two positively charged particles are shown as circles, the red particle is traveling out of the page, the green particle is traveling into the page. The forces experienced by each particle due to the magnetic field are shown as blue arrows.

The force which accelerates the particles is provided by radio-frequency cavities such as in figure 1.3, of which the LHC has 16 [1] The electric field in the radio-frequency cavity forms a standing wave, the separation between bunches of particles to be accelerated must be matched to the frequency of this wave. Protons in the LHC are accelerated in bunches and in vacuum, this to increase the likelihood of collisions and mitigate loss of energy and scattering effects due to interactions with air molecules. These two factors lead to the occurrence of space charge which causes

an increase in the emittance of the beam, where the emittance is defined as the total area that the beam occupies in its beam-pipe. The greater the energy of the particles the more they can overcome increase in emittance due to space charge. Increased emittance is especially problematic in circular accelerators where periodic effects can quickly lead to the loss of beam. For these reasons it would be very challenging to accelerate protons from rest in a synchrotron, the starting point for the protons of the LHC is therefore a linear accelerator called Linac2 [? ] which is used to overcome space charge effects before the protons move on to a series of synchrotrons as seen in figure ??.

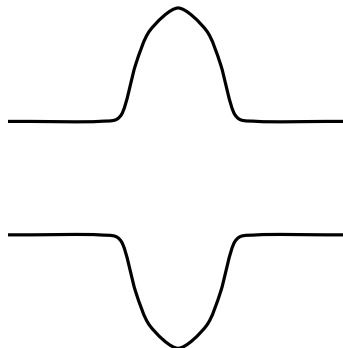


Figure 1.3: A representation of a radio-frequency cavity where the electric field lines are shown in black.

Even a beam with its emittance under control would still be lost from the accelerator if only dipole magnets were used to control its path. Magnets in a quadrupole configuration as in figure 1.4 are used to focus the beam and keep it in the beam-pipe. The quadrupoles behave such that particles feel a force that increases with the distance from the centre of the beam leading to simple harmonic motion of individual particles in a bunch. The LHC has a series of 24 quadrupole magnets each for focusing in the horizontal and vertical directions [1] as well as higher multipolarity configurations; sextupole, octupole, decapole and dodecapole which are used to correct imperfections in the fields of other magnets.

The statistical nature of particle physics analyses means that larger datasets (more recorded collisions) increase the sensitivity of searches and measurements. Constraints on the number of years the LHC is able to run for mean that the best way to record more collisions is to collide more particles per second. A quantity

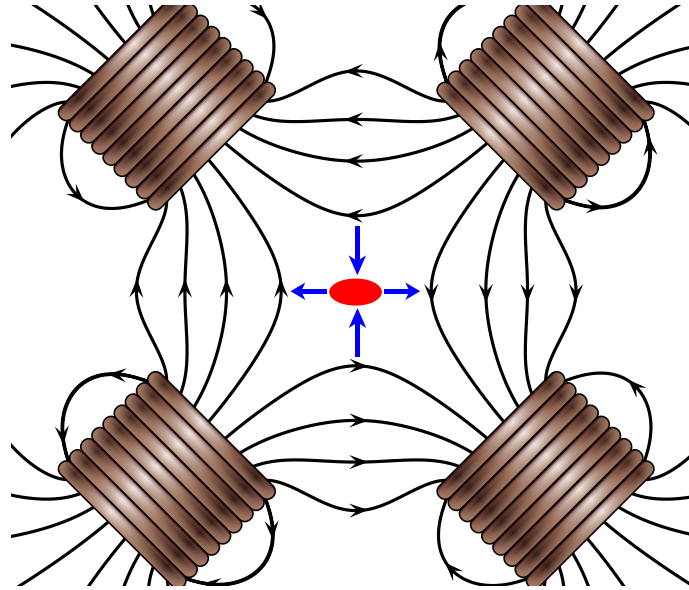


Figure 1.4: Representation of an idealised set of coil magnets in a quadrupole configuration with a proton beamspot shown as a red ellipse. The proton beam is drawn coming out of the page (*watch out!*), magnetic field lines are drawn in black and the forces acting on each bunch of protons are drawn as blue arrows.

known as the luminosity is often used to describe how much data is available for an analysis, it is written as

$$L = \frac{1}{\sigma} \frac{dN}{dt}, \quad (1.2)$$

where  $\sigma$  is the cross-section, a volume within which particles must pass by one another in order to interact, and  $N$  is the number of events recorded in a period of time  $t$ . For luminosity at the LHC  $N$  can be expressed as

$$N = n_{bp} n_1 n_2 \nu_r, \quad (1.3)$$

where  $n_{bp}$  is the number of colliding bunch pairs,  $n_1$  and  $n_2$  are the number of protons in each beam and  $\nu_r$  is the frequency with which the beams rotate around the LHC's circumference. The number of particles in the beams is limited by space charge. The number of bunches is limited by the frequency that the radio-frequency cavities can operate at. The revolution frequency is limited by the strength of the dipole magnets and the circumference of the accelerator ring. Increasing luminosity by reducing the cross-section amounts to reducing the beam widths which is limited by the emittance of the beam. The LHC has already exceeded its design luminosity

providing physicists with more data to analyse than expected and plans are well underway for the upgrade to a High-Luminosity LHC (HL-LHC) [12].

## 1.2 The ATLAS Detector

The ATLAS detector [13] resides at a location on the LHC ring called Point 1, its full name is A Toroidal LHC ApparatuS. A diagram of the detector is shown in figure 1.5. ATLAS is considered to be a general purpose particle detector and has a wide physics program including: Higgs boson physics, top quark physics, searches for Supersymmetry and exotic states, probes of CP violation in b-quarks and light states and heavy ion physics. The detector itself is very large in size, spanning a width of 25 m and a length of 44 m and weighs 7000 tonnes which is comparable to the weight of the wrought iron content of the Eiffel tower [14].

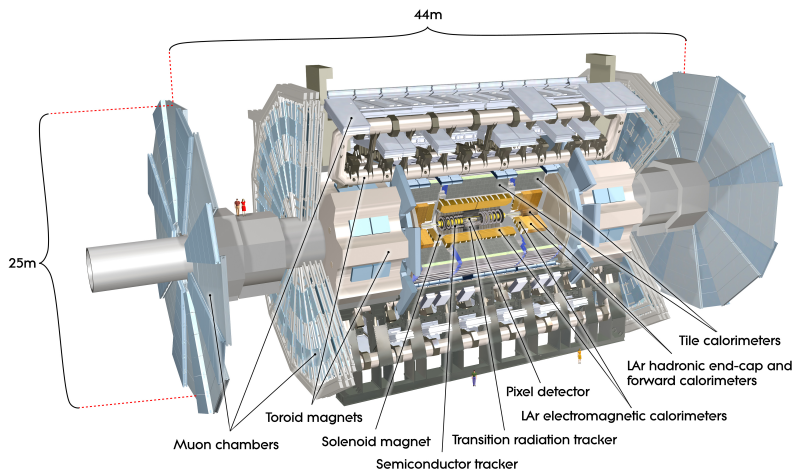


Figure 1.5: Computer generated image of the whole ATLAS detector with the major sub detectors labeled [15].

Due to the composite nature of the proton, the decay products of collisions are extremely numerous. Additionally when two bunches of protons cross there is the chance that more than one hard scattering event occurs and softer glancing collisions are also a possibility. The number of hard scattering events in a given bunch crossing is known as the pile-up of the collision and is often denoted with the symbol  $\mu$ . As can be seen by inspecting equations 1.3 and 1.2 increasing the luminosity will often

cause a higher pile-up environment in the detector. The variety of decay products of each collision necessitate the use of specialised sub-detectors in order to accurately measure the output of collisions. There are dedicated sub-systems in ATLAS with the purpose of measuring properties of specific classes of particles. Ultimately in all cases a digital electrical signal is the desired output of a sub-detector which usually originates as an analogue signal. It is interesting to note that despite the many charges that are associated with the forces of nature discussed in chapter ?? the only one that we can directly measure is electric charge.

The ATLAS sub-systems are located in either the barrel of the detector or one of the end-caps. These two areas have a different geometry, and due to their relative positions with respect to the beam-pipe are exposed to different amounts of radiation, so the design of a sub-system in the barrel will differ from that of a sub-system measuring the same quantities in the end-cap. The details that follow are based on the ATLAS technical design report volumes [16, 17] unless another citation is present. Before detailing individual components it is important to detail certain properties of the detector relevant to all sub-systems. The coordinate system used to describe the ATLAS detector is known as right-handed. Three orthogonal axes ( $x, y, z$ ) are used to describe the 3D space of the detector. The x-axis points towards the centre of the LHC ring, the y-axis points upwards and the z-axis points along the LHC beam pipe y-axis. The three axes meet at the interaction point which is the nominal position where bunches cross, located in the centre of the detector. Cylindrical coordinates  $(r, \phi)$  are also often used to describe the physical features of the detector and phenomena caused by interactions in the detector that shall be referred to as analysis objects. Their definitions are that  $\phi$  is the azimuthal angle in the x-y plane (transverse) around the beam pipe and  $r$  is the distance from the interaction point. A relativistic invariant analogy to the zenith angle of an object measured from the z-axis is pseudo-rapidity  $\eta = -\ln(\tan(\theta/2))$  where  $\theta$  is the ordinary zenith angle measured from the same axis.

By inspecting equation 1.1 it is clear that neutral particles for which  $q = 0$  do not experience the Lorentz force. However for charged particles, as previously discussed,

a magnetic field alters the trajectory of the particle whilst preserving its energy. A large portion of the ATLAS detector is immersed in magnetic fields created by the magnet systems, and so this deflection phenomenon is present and exploited when making measurements of charged particles. There are four magnet systems in ATLAS the solenoid, the barrel toroid, and two end-cap toroids. The solenoid surrounds the inner detector whilst the toroid systems surround the muon chambers. Figure 1.6 shows a heat map of the magnetic field strengths within ATLAS, the image is from an article detailing the superconducting magnet system [18]. The magnet systems store a total energy of 1.6 GJ and produce fields of a combined volume of approximately  $12 \times 10^4 \text{ m}^3$ .

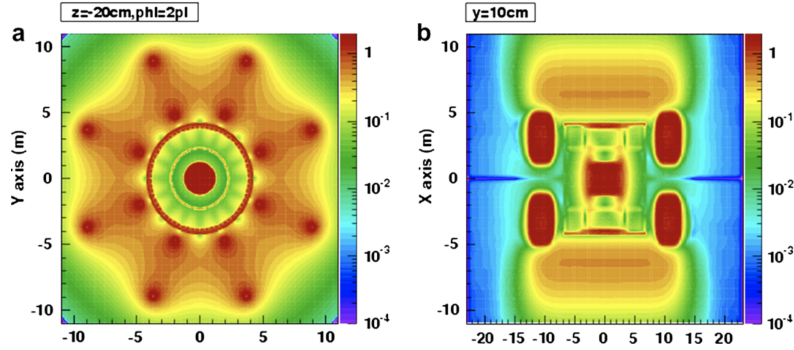


Figure 1.6: ATLAS magnetic field profile, showing a transverse cross-section in the centre of the detector (a), and a longitudinal section (b) [18].

## Tracking: The Inner Detector

The Inner Detector (ID) is comprised of a number of different tracking detector sub-systems; the pixel detectors, the semiconductor tracker (SCT) and a transition radiation tracker (TRT) as seen in figure 1.9. It covers a volume corresponding with the total  $\phi$  angle. The pixel detectors and SCT cover the range  $|\eta| < 2.5$  and the TRT covers  $|\eta| < 2.0$ . The job of the ID is to track the propagation of charged particles through the detector. This is achieved by measuring a sequence of hits for each charged particle that propagates through its volume. The sequence of hits describing the trajectory of a given charged particle must be disentangled from other hits in the detector, track-finding algorithms are applied to this end. Using these

tracks we can measure; the direction of the particle, the sign of the electric charge of the particle, the rate of energy loss of the particle with respect to its distance traveled and by constructing the sagitta the transverse momentum of the particle (denoted  $p_T$ ). An example construction of the sagitta is shown in figure 1.7 and its relation to  $p_T$  is

$$S = \frac{qL^2B}{8p_T}, \quad (1.4)$$

where  $L$  is the distance between the first and last hits in the track,  $q$  is the charge of the particle, and  $B$  is the strength of the magnetic field, in this case the field produced by the solenoid magnet system. The system is made of a single layer

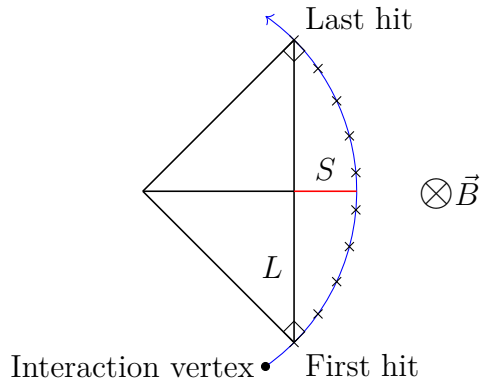


Figure 1.7: A diagram showing the geometric construction of the sagitta ( $S$ ) of a track. The track is comprised of a sequence of hits marked by crosses and the “lever-arm” distance between the first and last hit in the track is marked  $L$ . Charged tracks in a magnetic field pointing into the page, as shown, form arcs of circles. The two lines marked as normal to the track are radii of the circle to which this track’s arc belongs.

coil with an inner diameter of 2.46 m and produces 2 T field in the axial direction with respect to the beam-pipe. Using multiple tracks interaction vertices can also be reconstructed, the vertex which comes from the highest energy collision in a given event is known as the primary vertex. Vertices coming from pile-up and glancing collisions of partons also need to be reconstructed in order to separate detector response due to these collisions from that of the primary vertex. So-called impact parameters  $d_0$  and  $z_0$  are used to identify secondary and pile-up vertices, their construction is shown in figure 1.8. These parameters are also used to perform identification of particles within the detector such as  $b$ -quarks and  $\tau$ s. Tracks are

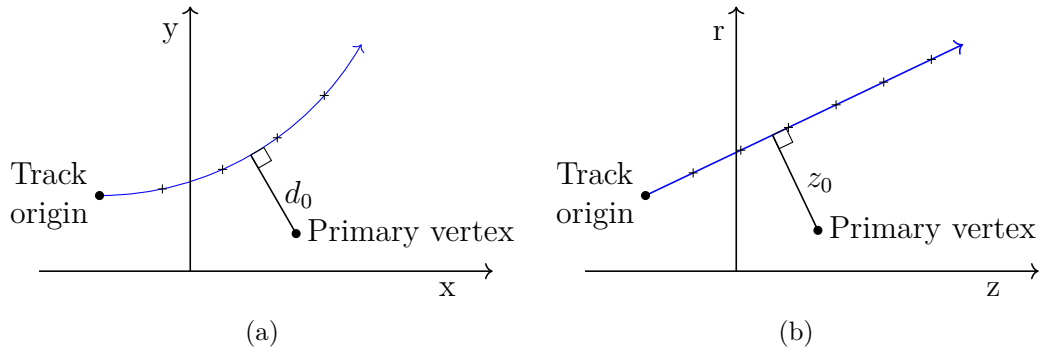


Figure 1.8: A diagram showing the geometric construction of the impact parameters  $d_0$  and  $z_0$ .

also used to calculate the calorimeter impact point and in general match activity in outer regions of the detector to an interaction vertex.

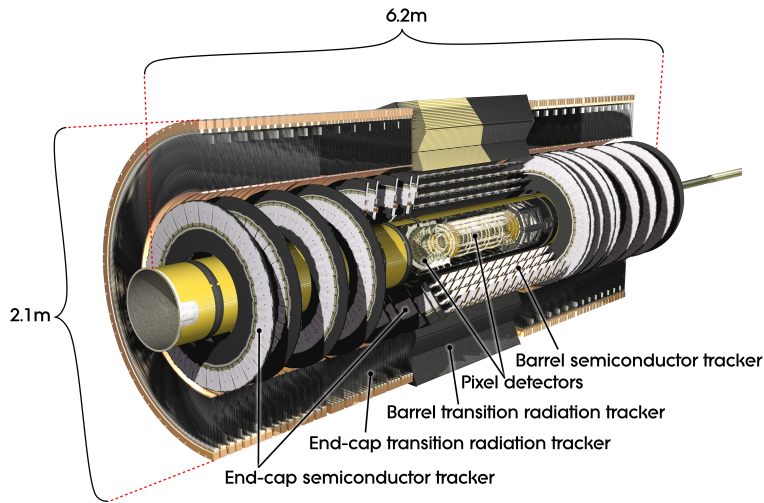


Figure 1.9: Computer generated image of the ATLAS inner detector [19].

With the exception of the TRT the tracking sub-systems are silicon based detectors. The silicon detection medium acts as a reverse bias diode. Charged particles incident on the silicon cause ionisation in the depletion layer. The products of this ionisation are electrons and holes (excess pockets of positive charge in the silicon) which produce a signal that must be handled by a read-out system. The signal is referred to as the charge collected. Application-specific integrated circuits (ASICs) are used to readout the signal performing the analogue to digital conversion. The combination of the detection medium, readout system and the printed circuit board

(PCB) on which they are joined is referred to as a module.

## Pixel Detectors

There are four layers of pixel detectors that are the closest components of the ID to the beam-pipe. Pixel detectors are silicon detectors where the diodes are approximately square in shape, giving the benefit of being able to resolve hits in two directions. The design originally had three layers, each  $250\ \mu\text{m}$  thick with  $50\ \mu\text{m}$  by  $250\ \mu\text{m}$  pixels, of oxygen doped n-type silicon crystals. During LS1 a fourth layer, closest to the beam-pipe (which was also replaced for a smaller radius version) was added. This layer is known as the insertable B-layer (IBL) [20], the motivation for its addition was to counteract degradation of original performance of the ID due to irreversible damage by radiation. As well as the inclusion of the IBL, performance degradation is mitigated by increasing the bias voltage across the pixels from 100 V (their starting voltage) to up to 600 V. Additionally the IBL being closer to the beam-pipe allows for interaction vertices to be measured more precisely. The need for better reconstruction of vertices is motivated by their role in the performance of algorithms that classify jets of activity in the detector that are initiated by B-hadrons, this is where the IBL gets its name. There are no pixel detectors in the end-caps. Each pixel is small in size which mean many can fit on one module, all requiring their own conductor for readout. The solution to this challenge is to use a complex process known as bump bonding, which is both expensive and time consuming.

## Semiconductor Tracker

Next closest to the beam-pipe is the SCT whose modules have long thin strip shaped diodes. The strips provide high resolution in only a single direction. In contrast to the n-type silicon of the pixels, the strips are made from p-in-n type silicon. Each SCT module is comprised of two back to back wafers such that the orientation of the strips are offset by a small angle in order to improve coverage. Each strip is covered in a metalised layer, the strips are separated by a distance of  $80\ \mu\text{m}$ . A rather old

and dirty SCT module left over from the quality control testing stage of production that took place at Queen Mary University of London can be seen in figure 1.10. As can be seen in the figure the SCT modules are wire bonded to their ASICs which is cheaper and faster than the bump bonding used on the pixel modules. In order to

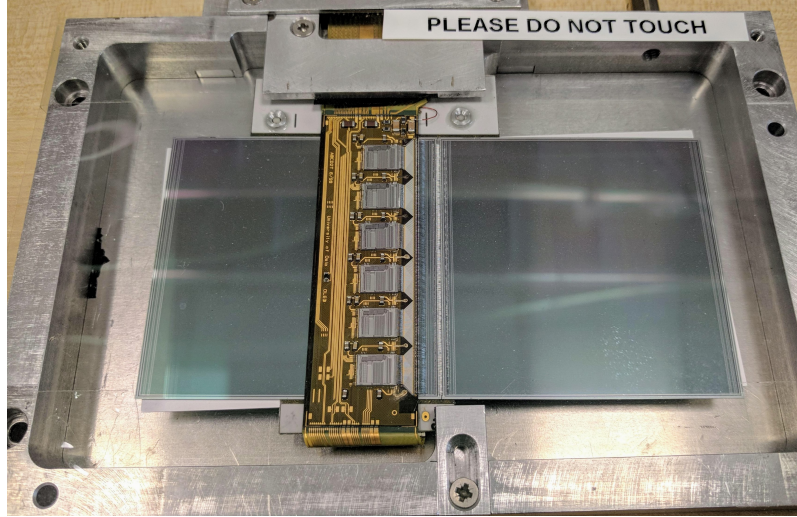


Figure 1.10: An image of an SCT long strip module mounted in a rig for testing at Queen Mary University of London.

calibrate the response of the strips a  $100\text{ M}\Omega$  poly-silicon resistor is located at the end of each strip. Figure 1.11 shows an image of the snake-like structure of a poly-silicon resistor from the end of an SCT module. The modules come in two different

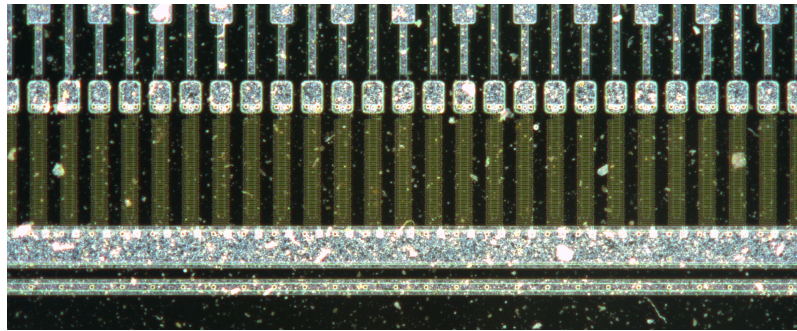


Figure 1.11: A close up image of the end of an SCT sensor in which the snake-like poly-silicon resistors are visible as a yellowish coloured structure at the end of each strip. This image was taken with a high resolution automatic area scanner commissioned by the author [21] in order to take full scans of strip sensors during the production of the ATLAS Inner Detector upgrade known as the Inner Tracker (ITk) [22, 23].

designs, short strips and long strips with the short strips forming the layer closest to the pixel detectors and the long strips on the outside. The original operating

bias voltage was 150 V but again due to radiation exposure this will raise to up to 350 V over time as necessary. There are four layers of semiconductor trackers in the barrel arranged so that sensors have a tilt with respect to a perfect coaxial cylinders of approximately 11 °. This tilt increases the amount of material that particles will travel through and is optimized to the geometry of the detector. Similarly the end-cap modules are arranged in petal like structures, with a number of different geometric designed based on the position within the end-cap.

### Transition Radiation Tracker

The final layer of the ID is the TRT, the primary role of the TRT is to aid electron identification by measurement of transition radiation. The TRT is mostly made up of polyimide drift tubes with a diameter of 4 mm. The drift tubes are filled with a gas mixture whose majority constituent is xenon. These tubes operate with a voltage of -1530 V and are contained within a carbon fibre support structure. The geometric layout of the tubes is optimised individually for the barrel and end-caps.

### Calorimeters

The purpose of the calorimeters is to measure the total energy of particles that pass through their volume, this is achievable only if the calorimeter stops the particle completely. A desirable side effect is that they also act as a barrier to stop particles passing through to the muon spectrometers, of course this means necessarily that muons pass through the calorimeters. There are two calorimeter systems in ATLAS the electromagnetic calorimeter (ECAL) and the hadronic calorimeter (HCAL), they will be explained in the following sections. The calorimeters are not immersed in a significant magnetic field compared to the rest of the ATLAS as seen in the heat map of figure 1.6. The geometric layout of the calorimeter systems, as well as the location of specific components can be seen in figure 1.12, in which the ID can also be seen (greyed out). Information from the two calorimeters is used in conjunction for any particles whose decay products propagate through both volumes. Both calorimeters

are split up into cells of material that are used to determine the position of decay products in the detector.

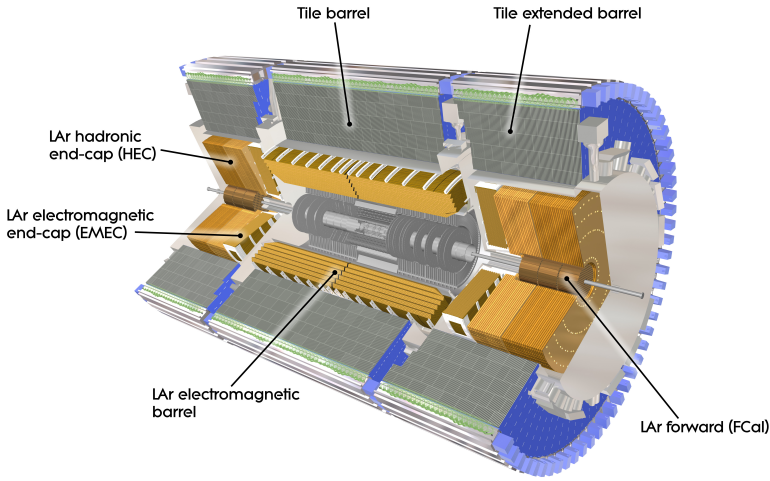


Figure 1.12: Computer Generated image of the ATLAS calorimeter [24].

High energy physics calorimeters function by measuring the shower of particles that are produced as a result of the incident particle losing its energy. Both calorimeters in ATLAS are sampling calorimeters, meaning that they are comprised of alternating layers of absorber and detection medium. The purpose of the absorber medium is to provide a material in which particle showers evolve rapidly over a short distance, though they are in general not sensitive to measuring those showers. The detection medium or active material is used to then measure those showers.

In general a good calorimeter will have the following properties. It should be hermetic meaning that there are no gaps for particles to escape through without being measured. It should have a fast response time to keep up with the rate of collisions (actually the rate of the trigger see the following section). It should be radiation tolerant in order to perform over a long period of time. It should be able to measure energy to a high resolution in order to resolve resonances over backgrounds and have a high granularity of cells in order to accurately determine the position of energy deposits (and aid particle identification). High energy resolution is greatly aided by not having anything front of the calorimeter which may change an incident particles energy before it strikes the calorimeter itself. This requirement is therefore

somewhat at odds with having a detector that has good  $pT$  resolution for electrons, positrons and photons (muons go all the way through the calorimeter anyway) due to the process by which  $pT$  is measured becoming more precise with a longer “lever-arm” distance  $L$  as seen in figure ?? and equation 1.4.

### Electromagnetic Calorimeter

The ECAL is primarily concerned with measuring the energy of electrons, positrons and photons. These particles primarily interact with the electromagnetic force and so produce electromagnetic showers when they lose their energy. The ECAL resides closer to the interaction point than the HCAL and has liquid argon (LAr) as its active material. LAr is a good choice for the calorimeter which is closer to the interaction point as it is naturally resistant to damage by radiation. The absorber of the ECAL is lead, it is suitable as it has a high number of nucleons ( $Z$ ) and the radiation length<sup>1</sup> of a given shower is inversely proportional to  $Z^2$ . An applied electric field causes ions produced in the EM shower to drift in such a way that the signal induced is proportional to the energy deposited by the incident particle.

### Hadronic Calorimeter

The HCAL end-caps use a LAr active material like the ECAL. The absorber is copper instead of lead and the dimensions are more suited to hadronic particle showers as opposed to electromagnetic. As noted before LAr is naturally radiation hard which is why it is used in the end-caps which see more radiation than the barrel regions due to almost all of the momentum of the colliding bunches of particles being in the axis of the beam-pipe. The barrel section of the hadronic calorimeter is made from scintilating tiles of active material interspersed with steel as an absorber. Scintillation is the process by which a scintillation medium produces light when energy particles travel through it. The amount of light produced is proportional to the energy of the incident particle that initiated the shower. In order to convert the

---

<sup>1</sup>The radiation length  $X_0$  is the thickness of material that reduces the energy of a particle by a factor of  $e$  the natural number.

light into a digital electrical signal photo-multiplier tubes (PMTs) are used. PMTs are able to measure very small amounts of light, even the incidence of a single photon. This is achieved by initially exploiting the photo-electric effect whereby the incident photon knocks an electron from a metallic part of the PMT. The current produced by this electron is then multiplied by a very large factor (up to  $10^8$  for some PMTs) by a series of dynodes (electrodes in vacuum that produce secondary emission).

## Muon Spectrometers

Surrounding the calorimeters are the muon spectrometers, which form the most outer layer of the detector. Though muons are charged leptons just like electrons, their specific properties mean that dedicated muon spectrometers are required to detect them. Muons deposit far less energy per distance traveled than other particles meaning that they punch through most materials with ease. As can be seen in figure 1.13 the components of the muon spectrometers are the thin-gap chambers, cathode strip chambers, resistive plate chambers and monitor drift tubes. The barrel and end-cap toroid magnets immerse the muon spectrometers in a magnetic field which at its peak (visible in figure 1.6) has a strength of 4 T. Despite a stronger peaking magnetic field than in the solenoid observed muon tracks are often far less curved than that of their lighter cousins, the electrons. This is due to the larger mass of the muon. Muons do leave tracks in the ID and also deposit small amounts of energy in the calorimeters. Tracks in the muon spectrometers are matched up to tracks in the ID with the aid of the location of energy deposits in the calorimeters if possible. The full tracking information for muons can be used in algorithms such as overlap removal, which is used to remove muons from jets that they have been erroneously associated with by matching the muon with its ID track.

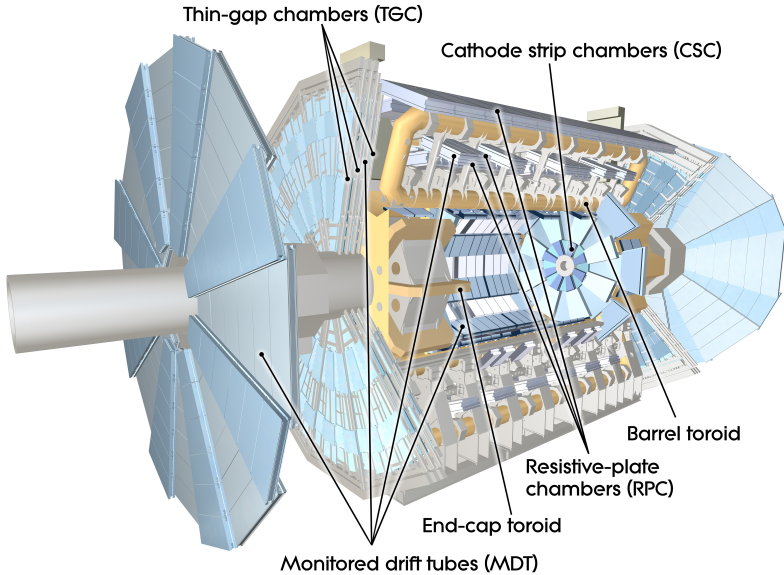


Figure 1.13: Computer generated image of the ATLAS Muons subsystem [25].

## Trigger Systems

The trigger systems in ATLAS allows data to be recorded only when an event meets certain criteria. Without triggering there would be no way to decide which events to readout and which to ignore. It would be impossible to readout every interaction that occurs in the detector. The reason for this is that the geometric constraints of the detector mean that there is only a small space available for readout wires, as detection medium needs to be prioritized for sensitivity and technology limits the data rate that one can achieve through a cable of fixed area. The trigger system comes in two parts, a hardware component referred to as level one (L1) and software component referred to as the high level trigger (HLT). The L1 system is comprised of the L1 calorimeter (L1Calo) trigger which operates by searching for clusters of energy in the calorimeters and the L1 muon (L1Muon) system which coincidences in the muon systems. A third system L1 topological (L1Topo) uses regions of interest built from the L1Calo and L1Muon data which are passed to central trigger processors for selection. The various limitations of the hardware mean that these selections must be passed up to the next level of triggering, the HLT in a time window of  $2.5 \mu\text{s}$ . The HLT takes information from the L1 systems and uses faster versions of an offline style analysis in order to select or reject events for readout. In

order for a trigger to fire an event must pass fully all of the requirements of one of the algorithms defined by an extensive trigger menu. More information about the triggers used in the  $VH(bb)$  analysis will be given in a later chapter.

# Bibliography

- [1] Oliver Sim Brüning, Paul Collier, P Lebrun, Stephen Myers, Ranko Ostojic, John Poole, and Paul Proudlock. *LHC Design Report*. CERN Yellow Reports: Monographs. CERN, Geneva, 2004. URL <https://cds.cern.ch/record/782076>.
- [2] *LEP design report*. CERN, Geneva, 1984. URL <https://cds.cern.ch/record/102083>. Copies shelved as reports in LEP, PS and SPS libraries.
- [3] CERN. ATLAS: Letter of intent for a general purpose p p experiment at the large hadron collider at CERN. 1992.
- [4] M. Della Negra et al. CMS: letter of intent by the CMS Collaboration for a general purpose detector at LHC. Technical Report CERN-LHCC-92-003. LHCC-I-1, CERN, Geneva, 1992. URL <https://cds.cern.ch/record/290808>. Open presentation to the LHCC 5 November 1992, M. Della Negra/CERN, CMS Spokesman.
- [5] H. Dijkstra, Hans Jürgen Hilke, Tatsuya Nakada, and Thomas Ypsilantis. LHCb Letter of Intent, LHCb Collaboration. 1995.
- [6] Letter of Intent for A Large Ion Collider Experiment [ALICE]. Technical Report CERN-LHCC-93-016. LHCC-I-4, CERN, Geneva, 1993. URL <https://cds.cern.ch/record/290825>.
- [7] G Giacomelli, A A Faust, and James L Pinfold. A search for highly ionizing particles and slow exotic decays at the LHC using the MOEDAL detectors:

- letter of intent. Technical Report CERN-LHCC-98-05. LHCC-I-19, CERN, Geneva, Feb 1998. URL <https://cds.cern.ch/record/347906>.
- [8] W Kienzle, , et al. *Total cross section: elastic scattering and diffraction dissociation at the LHC.* Letter of Intent. CERN, Geneva, 1997. URL <http://cds.cern.ch/record/335255>.
- [9] O Adriani. LHCf Letter of Intent for a p-Pb run. A precise study of forward physics in  $\sqrt{s_N N} = 4.4$  TeV proton-Lead ion collisions with LHCf at the LHC. Technical Report CERN-LHCC-2011-015. LHCC-I-021, CERN, Geneva, Dec 2011. URL <https://cds.cern.ch/record/1404163>.
- [10] Christiane Lefèvre. The CERN accelerator complex. Complexe des accélérateurs du CERN. Dec 2008. URL <https://cds.cern.ch/record/1260465>.
- [11] Design Report Tevatron 1 project. Technical Report FERMILAB-DESIGN-1984-01, 1984. URL <https://cds.cern.ch/record/1478620>.
- [12] I. Bejar Alonso and L. Rossi. HiLumi LHC Technical Design Report. 2015.
- [13] Georges Aad et al. (ATLAS Collaboration). The atlas experiment at the cern large hadron collider. *Journal of Instrumentation*, 3(08):S08003, 2008. URL <http://stacks.iop.org/1748-0221/3/i=08/a=S08003>.
- [14] David Hanser. *Architecture of France*. Greenwood Press, Westport, Conn, 2006. ISBN 978-0-313-31902-0.
- [15] Joao Pequenao. Computer generated image of the whole ATLAS detector. Mar 2008. URL <https://cds.cern.ch/record/1095924>.
- [16] A. Airapetian et al. ATLAS: Detector and physics performance technical design report. Volume 1. 1999.
- [17] A. Airapetian et al. ATLAS: Detector and physics performance technical design report. Volume 2. 1999.

- [18] H.H.J. ten Kate. The atlas superconducting magnet system at the large hadron collider. *Physica C: Superconductivity*, 468(15):2137 – 2142, 2008. ISSN 0921-4534. doi: <https://doi.org/10.1016/j.physc.2008.05.146>. URL <http://www.sciencedirect.com/science/article/pii/S0921453408004541>. Proceedings of the 20th International Symposium on Superconductivity (ISS 2007).
- [19] Joao Pequenao. Computer generated image of the ATLAS inner detector. Mar 2008. URL <https://cds.cern.ch/record/1095926>.
- [20] M Capeans, G Darbo, K Einsweiller, M Elsing, T Flick, M Garcia-Sciveres, C Gemme, H Pernegger, O Rohne, and R Vuillermet. ATLAS Insertable B-Layer Technical Design Report. Technical Report CERN-LHCC-2010-013. ATLAS-TDR-19, Sep 2010. URL <https://cds.cern.ch/record/1291633>.
- [21] Thomas Paul Charman, Bart Hommels, and Adrian John Bevan. Authorship Qualification Task: ATLAS ITk Sensor Scanner Documentation (QMUL). Technical Report ATL-COM-ITK-2019-018, CERN, Geneva, Jan 2019. URL <https://cds.cern.ch/record/2674404>.
- [22] Ben Brueers. The design and layout of the Phase-II upgrade of the Inner tracker of the ATLAS experiment. Jul 2019. URL <https://cds.cern.ch/record/2681301>.
- [23] John Stakely Keller. The ATLAS ITk Strip Detector System for the Phase-II LHC Upgrade. Feb 2019. URL <https://cds.cern.ch/record/2663172>.
- [24] Joao Pequenao. Computer Generated image of the ATLAS calorimeter. Mar 2008. URL <https://cds.cern.ch/record/1095927>.
- [25] Joao Pequenao. Computer generated image of the ATLAS Muons subsystem. Mar 2008. URL <https://cds.cern.ch/record/1095929>.